



OPEN

Tunable sulphur doping on CuFe_2O_4 nanostructures for the selective elimination of organic dyes from water

Anam Aslam, Muhammad Zeeshan Abid, Khezina Rafiq, Abdul Rauf & Ejaz Hussain

In this work, sulphur doped copper ferrites ($\text{S-CuFe}_2\text{O}_4$) photocatalysts were successfully synthesized for the first time using the facile hydrothermal method. The as-synthesized photocatalysts were characterized through XRD, Raman, TGA, FT-IR, UV-Vis-DRS, SEM, EDX and PL techniques. The results revealed that doping with sulphur has been found to be a suitable alternative that causes strain in the lattices as anions replace the oxygen from the CuFe_2O_4 nanostructures. Due to sulphur dopants, photocatalysts are able to efficiently trap and transfer the photoinduced charges, which readily suppress charge recombination. A UV-Vis spectrophotometer was used to monitor the degradation of selective toxic organic dyes (RhB, CR, MO, and CV) in aqueous media. The dye degradation results provide evidence for the surprisingly superior performance of $\text{S-CuFe}_2\text{O}_4$ over pristine CuFe_2O_4 . On the basis of its efficiencies, this work can be assigned as an excellent candidate for photocatalysis science.

Water pollution is one of the world's most serious environmental problems. Industrialization produces wastewater that contains a variety of harmful pollutants¹. The most prevalent pollutants are synthetic organic dyes, which are widely used in variety of industries, and pose severe threats to the aquatic environment². Azo dyes that are widely used in textile industries are proven to be carcinogenic and killers for liver cells³. Similarly, methyl orange (MO) and crystal violet (CV) are toxic, water-soluble anionic azo dyes with complex chemical structures that cause gastrointestinal, respiratory, and skin irritations. Congo red (CR) is an azo dye that is carcinogenic, mutagenic, and causes reproductive problems⁴. Rhodamine B (RhB) is a fluorescein dye that causes skin and eye irritation and is toxic if swallowed. These fluorescein dyes are extremely cytotoxic to mammalian tissues and cause morphological and genetic changes^{5,6}. Thus, polluted water is becoming a challenge, especially for the urban communities lying near industrial zones. Therefore, it is crucial to remove these dyes from wastewater using an economical approach^{7,8}.

Various strategies have been developed for the degradation of dyes in contaminated water. Adsorption, electrochemical deposition, redox reactions and biological treatment are examples of these methods^{9,10}. However, due to the inherent toxicity, production of secondary pollutants and high cost of these approaches, these methods proved ineffective¹¹. More research is obligatory to develop cost-effective, stable and risk-free materials to address these issues. Photocatalytic dye degradation is a low-cost, versatile and energy-efficient process that breaks down organic dyes in water using light and a catalyst^{12,13}. For this purpose, various metal oxides, sulphides, quantum dots, noble metal nanoparticles, polymers, metal and non-metal doped hybrid materials, graphene-based materials, gold nanoclusters and transition metal ferrites have been used^{14–24}. Among these, nanomaterials of transition metal ferrites have low cost, high chemical stability, a large surface area, reusability and catalytic properties²⁵.

For dye degradation applications, a number of ferrites including spinel ferrites, have been reported to be used as catalysts²⁶. Thus, spinel ferrites are the type $\text{M}^{2+}\text{M}_2^{3+}\text{O}_4$ class of compounds that have attracted great attention for dye degradation studies^{27,28}. The typical formula for spinel ferrites is MFe_2O_4 , where $\text{M} = \text{Zn, Mn, Ni, Cu, etc.}$ The composition and structure of ferrites influence their ability to adsorb substances, which is dependent on their morphology and inherent crystal structure²⁹. CuFe_2O_4 is a spinel-type material with a narrow band gap, photochemical stability and visible light activity²⁸. Moreover, its low toxicity, cost-effectiveness, versatility, and recyclability make it an attractive catalyst for water purification applications^{30,31}. Various methods have been reported to synthesize spinel ferrites microstructures such as sol-gel, photo as well as electro deposition, solid

Institute of Chemistry, Inorganic Materials Laboratory 52S, The Islamia University of Bahawalpur, Bahawalpur 63100, Pakistan. ✉email: ejaz.hussain@iub.edu.pk

state reaction, hydrothermal method and coprecipitation³². Hydrothermal method is preferred due to versatility, uniformity, purity and ease of synthesis³³.

However, due to the rapid recombination of photo-generated charge carriers, it is necessary to improve the effectiveness of CuFe_2O_4 . To improve photocatalytic efficiencies, a variety of techniques, such as construction of nanocomposite³⁵, p-n junctions³⁶ and metals and non-metals doping³⁷ have been used. Selective doping can recast the band structure by generating quasi-stable energies³⁸. Recently, sulphur dopants on g- C_3N_4 , graphene sheets^{39,40} and ZnO have been reported to improve photocatalytic applications⁴¹. Moreover, because of the significant difference in size and electronegativity between S and O, S dopants modifies the optical, electrical and photocatalytic properties of semiconductor oxide⁴².

To modify the conventional ferrites and acquire the advantage of S-dopants, the hydrothermal method was adopted to synthesize S-doped copper ferrite ($\text{S-CuFe}_2\text{O}_4$) photocatalysts. The as-prepared CuFe_2O_4 and $\text{S-CuFe}_2\text{O}_4$ catalysts were used for degradation of the selective dyes like rhodamine B (RhB), congo red (CR), crystal violet (CV) and methyl orange (MO) as a probe reaction. The results demonstrate that $\text{S-CuFe}_2\text{O}_4$ photocatalysts demonstrate higher photocatalytic efficiencies as compared to pristine CuFe_2O_4 .

Experimental

Catalyst preparation. Copper ferrites were synthesized by hydrothermal method as follows: Solutions of 0.1 M copper nitrate and 0.2 M iron nitrate magnetic stirred for 30 min. After that, 0.01 M glucose solution was transfer to above solution and left it for stirring (22 h, 50 °C), the preparations of solutions were explained in (supporting information) section. The obtained mixture solution was then sonicated for 30 min by adjusting the sweep frequency (≈ 37 kHz, 300W). The final solution was kept in autoclave (Sanfa, DHG-9030) for 6 h at 140 °C, which is then cooled down and filtered by using high grade filter paper (WHA 1001325, Grade-1). The obtained precipitates were washed thoroughly using deionized water and then with absolute ethanol. To prepare sulphur doped copper ferrites ($\text{S-CuFe}_2\text{O}_4$), 500 mg of CuFe_2O_4 powder was transferred to autoclave reactor and appropriate amount of 1% thiourea solution (5 mg, 0.01 M) was added into this mixture and mixture was again kept in autoclave for 6 h at 140 °C. The synthesis scheme was illustrated in Fig. 1.

Characterization. To predict the morphology and crystal structures of $\text{S-CuFe}_2\text{O}_4$, powder X-ray diffraction (XRD) results were obtained at Philips-X Pertpro, with $\text{Cu } \alpha$ radiation, $\lambda = 1.5406$ Å. For the surface morphology of as-prepared catalysts, SEM analyses were conducted on a Field Emission Scanning Electron microscope (FEI-Nova Nano SEM-450). Energy dispersive X-ray analysis (EDX, Horiba 7593 H) afforded the chemical composition of the prepared catalysts. The ultraviolet-visible-diffuse reflectance (UV-Vis-DRS) results were obtained at AvaSpec-2048 TEC spectrometer. The Photoluminescence (PL) results were recorded using Fluorescence spectrometer (LS-45, Perkin Elmer), where PL intensities were measured at 300–650 nm range. Dye degradation experiments were performed using UV-Vis spectrophotometer (PerkinElmer/ λ -365). TGA was performed using TG209 F3Tarsus[®], NETZSCH Germany. Fourier Transform Infra-Red (FT-IR) analyses were performed on Bruker Tensor-27. Raman analysis was done by using JASCO NRS-5000/7000 dispersive Raman spectrometers.



Figure 1. Scheme used for the synthesis of CuFe_2O_4 and $\text{S-CuFe}_2\text{O}_4$.

Photocatalytic reactions. The photocatalytic degradation properties of pristine CuFe_2O_4 and $\text{S-CuFe}_2\text{O}_4$ were investigated in the presence of visible-light radiations within Pyrex reactor. The photoreactor was cylindrical, having a 500 mL volume capacity with an 8 cm internal and 10 cm external diameter. In order to prevent light emission into the surrounding environment, the outer wall of the reactor was covered by aluminum foil. The cool water was allowed to circulate around the walls of the reactor in order to keep it at room temperature. A halogen lamp having $\lambda > 400$ nm was used as a radiation source. The 10 mg amount of photocatalyst was fixed for each photoreaction at pH 7 for 15 ppm dye solution (vol = 100 mL). Prior to photoreaction, the solutions were stored in the dark (absence of light) to ensure the adsorption equilibrium. For the photoreaction, a halogen lamp was fixed at a distance of 30 cm from the reactor. The photocatalytic degradation efficiency was examined at different time intervals using a spectrophotometer (PerkinElmer/ λ -365).

Results and discussion

The synthesis procedure of our $\text{S-CuFe}_2\text{O}_4$ photocatalysts is shown in Fig. 1 (see details in the “Experimental” section). To remove the impurities and enhance the crystallinity, the as-synthesized photocatalysts were calcined at 350 °C for 3 h.

XRD. The phase purity and crystalline nature of as-prepared product was determined by XRD. The XRD pattern of copper ferrite nanostructures is shown in Fig. 2a. The XRD patterns exactly match the standard JCPDS file No. 77-0010⁴³. The diffraction peaks of as-synthesized catalysts are located at 18.34°, 30.17°, 35.54°, 37.18°, 43.19°, 53.59°, 57.13° and 62.744° that are associated with Miller indices as (111), (220), (311), (222), (400), (422), (511) and (440) respectively. These XRD patterns indicate that as-synthesized catalysts emphasize cubic spinel structures, where Fe^{+3} ions occupy octahedral while Cu^{+2} ions occupy tetrahedral sites. It has been noted that due to sulphur doping major peaks shifts to the lower 2 theta whereas intensity of diffraction peaks has been observed to be decreased as well. The XRD results depict that the replacement of larger sulphur anions was accomplished with the smaller oxygen ions in the CuFe_2O_4 structure. No other crystalline phases of Fe_2O_3 , FeS or CuS were detected that confirm the purity of the catalysts, some extra peaks beyond 65° were observed due to some CuO contents⁴⁴. The sharpness of peaks indicates that the designed catalysts of this work are highly

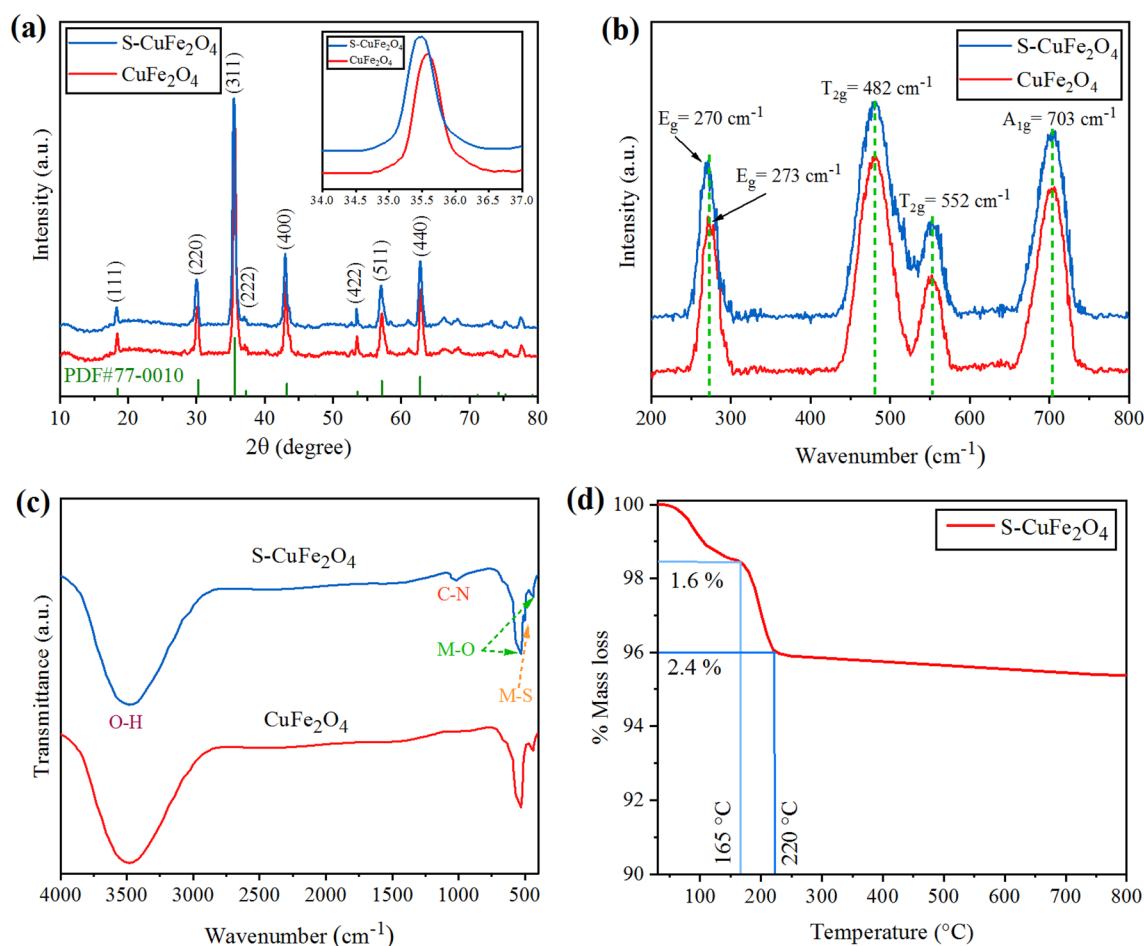


Figure 2. (a) XRD patterns exhibited with zoomed image in the inset, (b) Raman spectrum, (c) FT-IR spectrum of CuFe_2O_4 and $\text{S-CuFe}_2\text{O}_4$, (d) TGA of $\text{S-CuFe}_2\text{O}_4$ photocatalysts.

crystalline in nature. The crystalline sizes of pure CuFe_2O_4 and S- CuFe_2O_4 have been calculated by using Debye–Scherrer's Formula in Eq. (1).

$$D = \frac{0.94\lambda}{\beta \cos \theta} \quad (1)$$

where λ is 1.54060 Å, β is FWHM and θ is diffraction angle (Cu– $K\alpha$). The Williamson–Hall method was also used to calculate the crystallite size of both pure CuFe_2O_4 and S- CuFe_2O_4 Eq. (2).

$$\beta \cos \theta = \frac{K\lambda}{d} + 2 \varepsilon \sin \theta \quad (2)$$

where d is crystalline size, K is constant = 0.94, ε is constant = 1⁴⁵. The crystallite size (D) was calculated using the Scherer formula and Williamson–Hall method are tabulated in Table 1, whereas, the Williamson–Hall plots are depicted in Fig. S1.

Raman spectroscopy. Raman spectroscopy is an efficient technique for direct probe of structural transformation, cation redistribution, bonding in metal oxides and lattice distortion³⁰. Figure 2b represents Raman spectra of CuFe_2O_4 and S- CuFe_2O_4 . Group theory analysis yields four Raman active modes denoted by A_{1g} , E_g and two T_{2g} modes in range of 200–800 cm^{-1} ³¹. The A_{1g} mode observed at $\sim 703 \text{ cm}^{-1}$, E_g mode at $\sim 273 \text{ cm}^{-1}$, the two T_{2g} modes $\sim 482 \text{ cm}^{-1}$ and $\sim 552 \text{ cm}^{-1}$. The obtained Raman frequency relies on the Fe(Cu)–O bond length, that varies with the major factors, like phase transformation, lattice distortion and cationic redistribution³². It has been noted that sulphur dopants in copper ferrite shift the E_g mode slightly to a smaller wave number (273 to 270 cm^{-1}). Lattice distortion was observed, between two T_{2g} modes ascribed majorly due to the sulphur dopants as compared to oxygen contents present in catalysts³³.

FT-IR. The Fourier transforms infrared spectrum of CuFe_2O_4 and S- CuFe_2O_4 nanoparticles are shown in Fig. 2c. In the present work, major FTIR peak observed at 530 cm^{-1} is due to M–O vibration of tetrahedron where M represents copper or iron. Similarly, peak observed at 436 cm^{-1} was referred to the stretching of octahedron planes of spinel copper oxides. The broad band located at around 3500 cm^{-1} are related to bending vibration of O–H, which correspond to the hydroxyl groups or absorbed water molecules over the catalyst's surfaces. It is obvious that upon doping sulphur content, the metal sulphur vibrations lies at 500 cm^{-1} , exhibit low intensity than that of the Cu–O/Fe–O vibration peaks. FTIR patterns located approximately at 1020–1030 cm^{-1} is due to the C–N stretching, which are likely to be caused by thiourea⁴⁶. These stretching vibrations are also observed by other researchers working on S dopants⁴⁷. These nitrogen/carbon (N–C) vibrations are absent in the FT-IR spectra of pristine CuFe_2O_4 .

Thermo gravimetric analysis (TGA). Thermo gravimetric analysis of as-synthesized S- CuFe_2O_4 (without calcination) was performed to investigate physical behavioral changes (Fig. 2d). These evaluations were performed under N_2 atmosphere; within the temperature range 35–800 °C where increment in heating rate was maintained 5 °C/min. It has been observed that 1.6% weight loss was observed up to 165 °C, this loss can be attributed to the volatilization of absorbed water and solvent molecules⁴⁸. Moreover, further 2.4% weight loss up to 220 °C was observed, endorsed to decomposition of metal hydroxide^{48,49}. Afterwards, by increasing the temperature up to 800 °C no weight loss was observed, this exhibited excellent thermal stability of S- CuFe_2O_4 nanoparticles.

SEM with EDX analysis. The morphologies of pristine CuFe_2O_4 and S- CuFe_2O_4 nanostructures were investigated by SEM (equipped with ETD/TLD detector). The SEM images of pristine CuFe_2O_4 are demonstrated in Fig. 3a,b. The results show that the particles are agglomerated and have irregular flacks-like morphologies. The particles have a tendency to agglomerate in clusters due to the attractive forces (i.e., magnetic dipole–dipole)⁵⁰. Whereas, the SEM results of as-prepared S- CuFe_2O_4 catalysts are shown in Fig. 4a–d at different magnifications (i.e., 5 μm , 2 μm , 1 μm and 500 nm). It is clear from SEM results that by doping with sulphur, the flakes-like morphology of catalysts became more regular and agglomeration was reduced, which indicate the porosity of catalysts⁵¹. Thus, more active sites are available for photocatalytic reactions. These results depict that S-doping enhances the surface area and assist to increase the catalytic activity of CuFe_2O_4 . EDX analyses provide valuable information on the composition and distribution of elements. The EDX results of as-synthesized pristine CuFe_2O_4 and S- CuFe_2O_4 photocatalysts are illustrated in Figs. 3c and 4e, respectively. The EDX results reveal the relative amounts of copper, iron, oxygen and sulphur in the material that are tabulated in Table S1 and S2 for

| Sr. no. | Catalyst name | Crystal size Scherer method (nm) | Crystal size W–H method (nm) | Band gap (eV) |
|---------|------------------------------|----------------------------------|------------------------------|---------------|
| 1 | CuFe_2O_4 | 17.85 | 22.73 | 1.80 |
| 2 | S- CuFe_2O_4 | 18.54 | 24.01 | 1.78 |

Table 1. Comparison of crystallite sizes and band gap energies of as-synthesized photocatalysts.

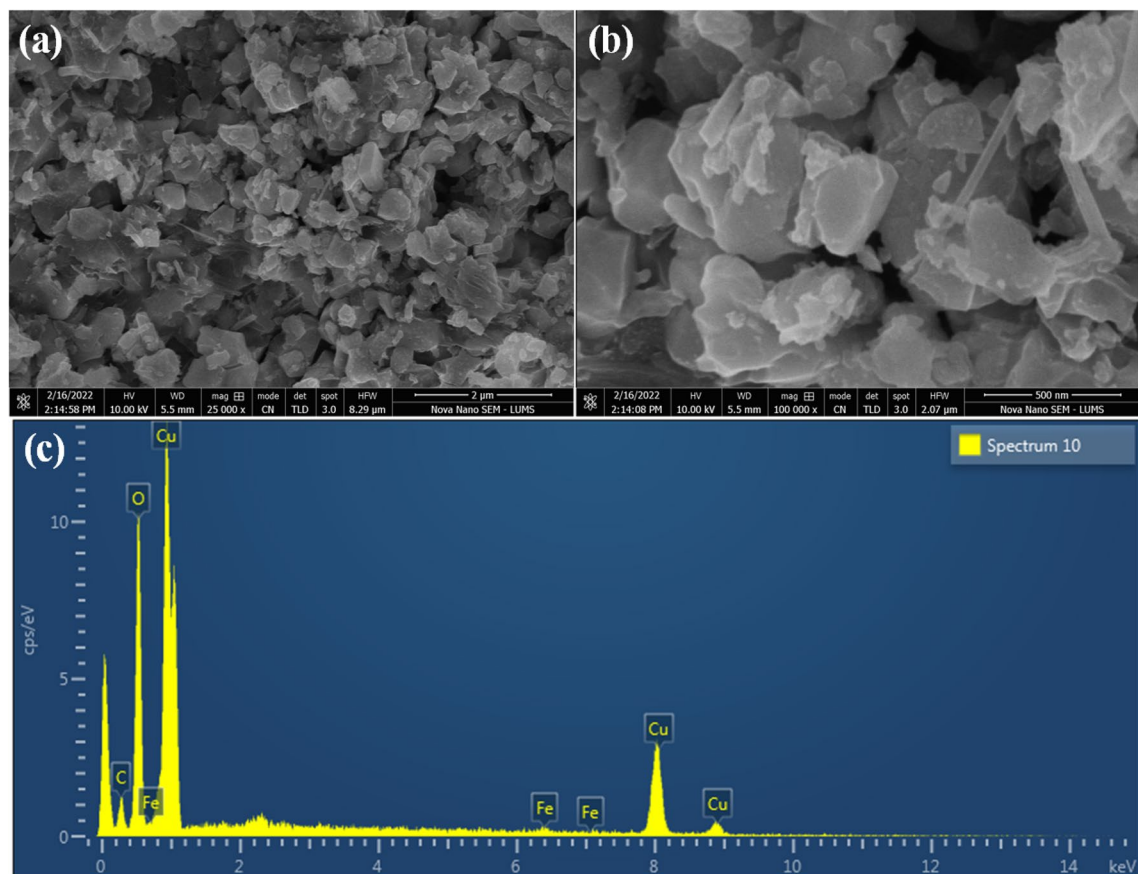


Figure 3. SEM images of pristine CuFe_2O_4 at (a) 2 μm , (b) 500 nm, (c) represents the EDX analysis.

pristine CuFe_2O_4 and S- CuFe_2O_4 photocatalysts respectively. Results have confirmed the purity and existence of sulphur dopants in CuFe_2O_4 photocatalysts.

UV–VIS–DRS. The optical properties of pristine CuFe_2O_4 and S- CuFe_2O_4 were investigated by their UV–Vis–DRS study. The UV–Vis–DRS has advantage over UV–Vis absorption spectroscopy specifically to obtain the optical properties of powdered sample because it has less scattering effects than the absorption of liquids⁵². Figure 5a illustrates an absorption edge that indicates the Urbach resemblance absorption tail within visible region^{53,54}. CuFe_2O_4 shows maximum absorption at ~ 688 nm, corresponding to its optical band gap i.e. $E_g = 1.80$ eV. Sulphur doping slightly red-shifted the visible absorption to around ~ 696 nm ($E_g = 1.78$ eV), showing excellent visible light response which results in higher photocatalytic activities, the band gap energy plot showed in Fig. 5b. The optimal band gap of pure and doped CuFe_2O_4 was determined by Eq. (3).

$$(\alpha h\nu)^2 = A(h\nu - E_g) \quad (3)$$

PL analysis. The photoluminescence (PL) of as-synthesized photocatalysts provides the fundamental information to determine the photo-induced electron–hole (e^-/h^+) pairs to trap and transfer processes. Figure 5c represents the comparative results for CuFe_2O_4 and S- CuFe_2O_4 which exhibit the broad peaks at 421 nm, 468 nm and 553 nm⁵⁵. The decrease in the intensity in case of S- CuFe_2O_4 indicates the sulphur incorporation⁵⁶. Moreover, this decrease intensity evidenced a greater transfer of electrons to active centers. PL peak at 468 nm corresponding to blue emission is due to imperative defects associated with the interface traps existing at the grain boundaries. Similarly, the peak at 553 nm corresponds to defect sites of oxygen vacancies. In S- CuFe_2O_4 emission is slightly shifted to 549 nm, attributed to the appearance of electronic levels of intrinsic characteristics⁵⁷. It specifies that back recombination of electrons and holes are remarkably lower in case of S- CuFe_2O_4 catalysts. Due to doping of sulphur, several mid-gap states are formed between valance bands as well as in conduction bands within the structures of prepared catalysts. These mid-gap energy states result in electron/hole pair separation successively because sulphur serves as a charge-separating center⁵⁸. In PL spectroscopy, a broader peak reveals better electron–hole separation, while high intensity peaks exhibit fast electron–hole recombination⁵⁹. It is obvious from the PL spectra that S- CuFe_2O_4 display highly enhanced photocatalytic performance due to an efficient charge carrier separation⁶⁰.

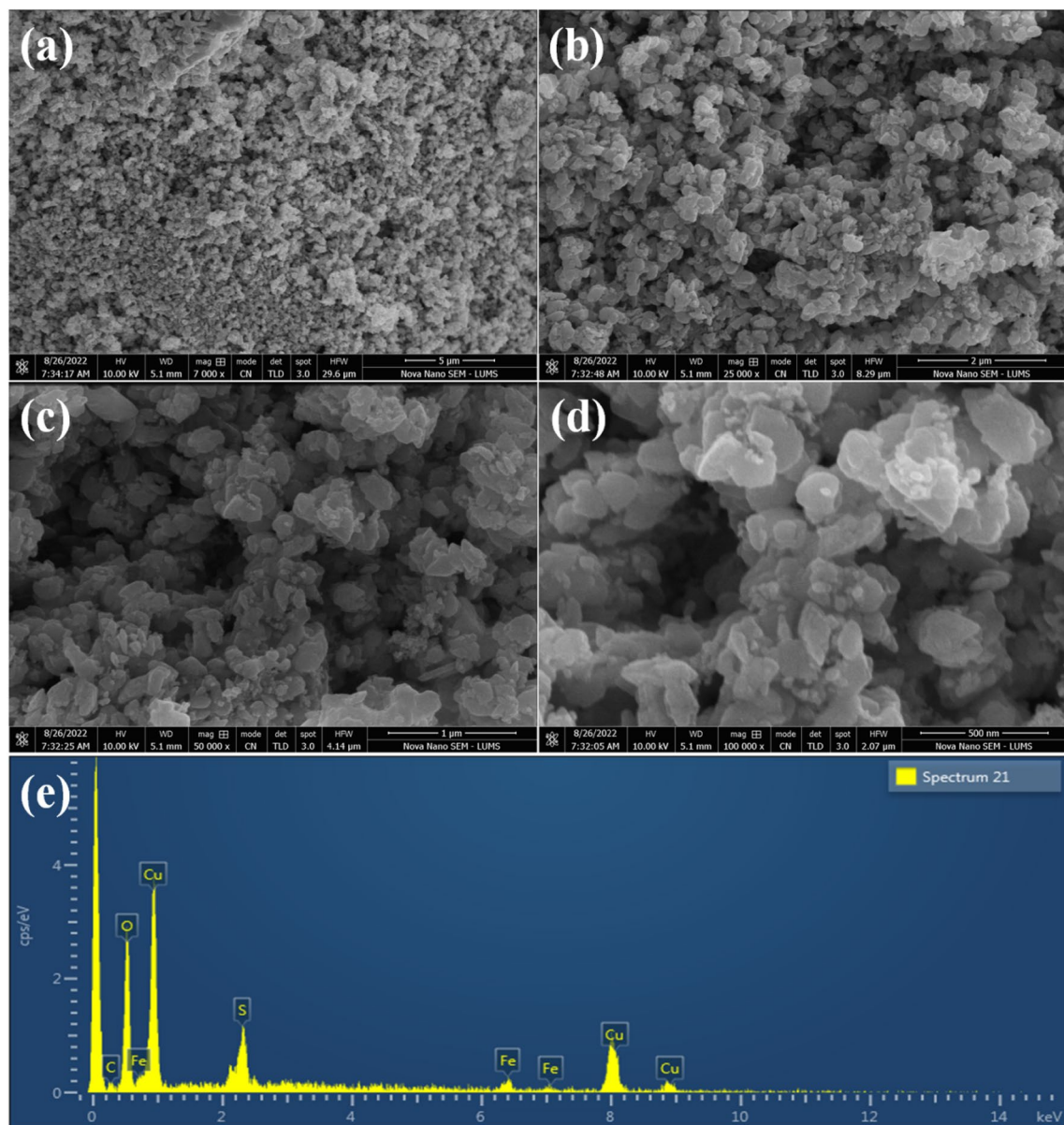


Figure 4. SEM images of S-CuFe₂O₄ at (a) 5 μm, (b) 2 μm, (c) 1 μm and (d) 500 nm, whereas (e) represents the EDX analysis.

Dye degradation studies. Figure 5d shows lambda max (λ -max) values for selective four toxic dyes such as CV, RhB, CR and MO having wavelength maxima at 590, 550, 500 and 460 nm respectively. The basic information and structure of selected dyes are demonstrated in supporting information. The degradation results of aforementioned dyes over as-prepared photocatalysts were monitored at different time intervals in 300–800 nm range. The results for the removal of RhB shown in Fig. 6a, indicate that S-CuFe₂O₄ photocatalysts adsorb 20.2% (302 mg/g) dye in the absence of visible light (dark). This adsorptive removal is accomplished without change in their λ -max. The amount of adsorbed dye at equilibrium q_e (mg/g) was calculated by using Eq. (4):

$$qe = (Co - Ce)V/m \quad (4)$$

where m is catalyst weight, V (L) is volume of solution and Co and Ce are concentrations at initial and equilibrium state of RhB solution⁶¹. Then sample was irradiated with visible light to examine the photocatalytic efficiency of the S-CuFe₂O₄. After 100 min, the concentration of degraded dye reached to ~99%. Comparison of degradation efficiency of pristine CuFe₂O₄ with S-CuFe₂O₄ shows 34% difference, see Fig. 7a. On the basis of PL and UV-VIS spectrophotometric studies, it could be concluded that presence of sulphur has enhanced the photocatalytic efficiency of copper ferrites by decreasing the electron hole recombination⁴⁷. Rhodamine B has one carboxylic acid (–COOH) and two amino groups (–NH₂). Ethyl molecules are electron promoters and donate electron to xanthene rings, as a result shifting the λ_{max} to higher wavelength⁶². The higher λ_{max} is due to electron donating effect of ethylene molecules. During the photoreaction, ethylene molecules are removed

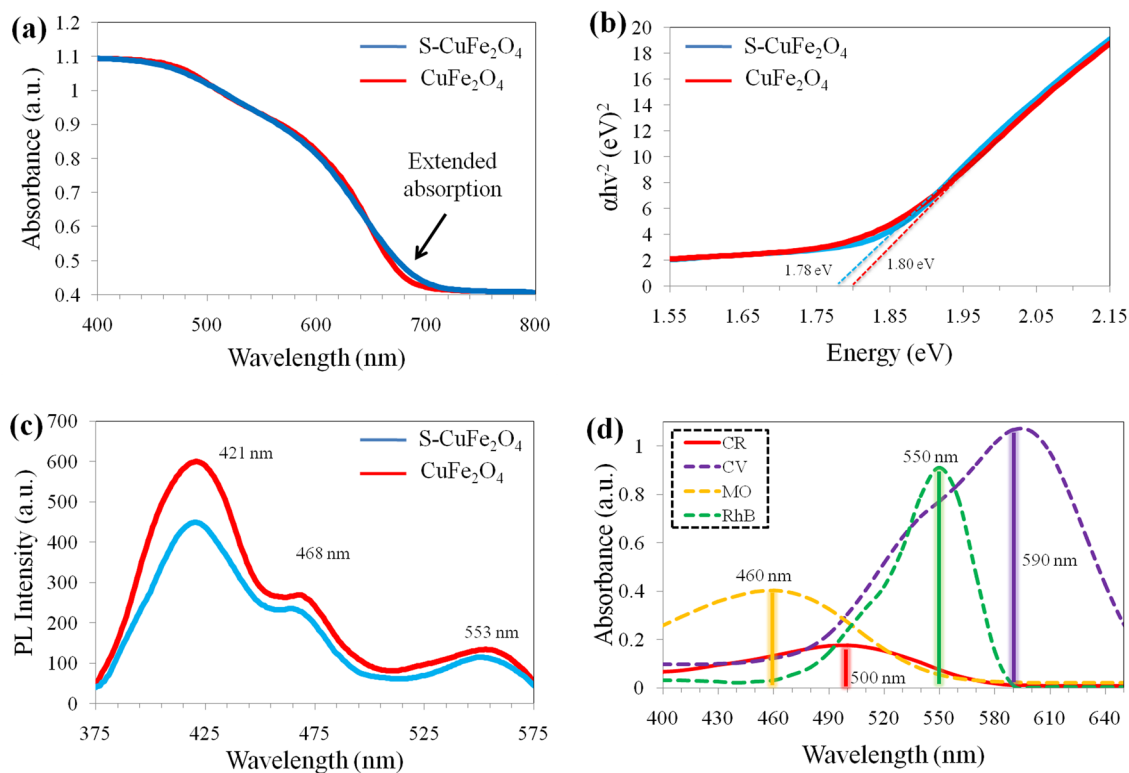


Figure 5. (a) UV-Vis-DRS (b) Band gap measurements for allowed transitions (c) PL results of CuFe₂O₄ and S-CuFe₂O₄ where (d) represents the λ_{\max} of CR, CV, MO and RhB dyes.

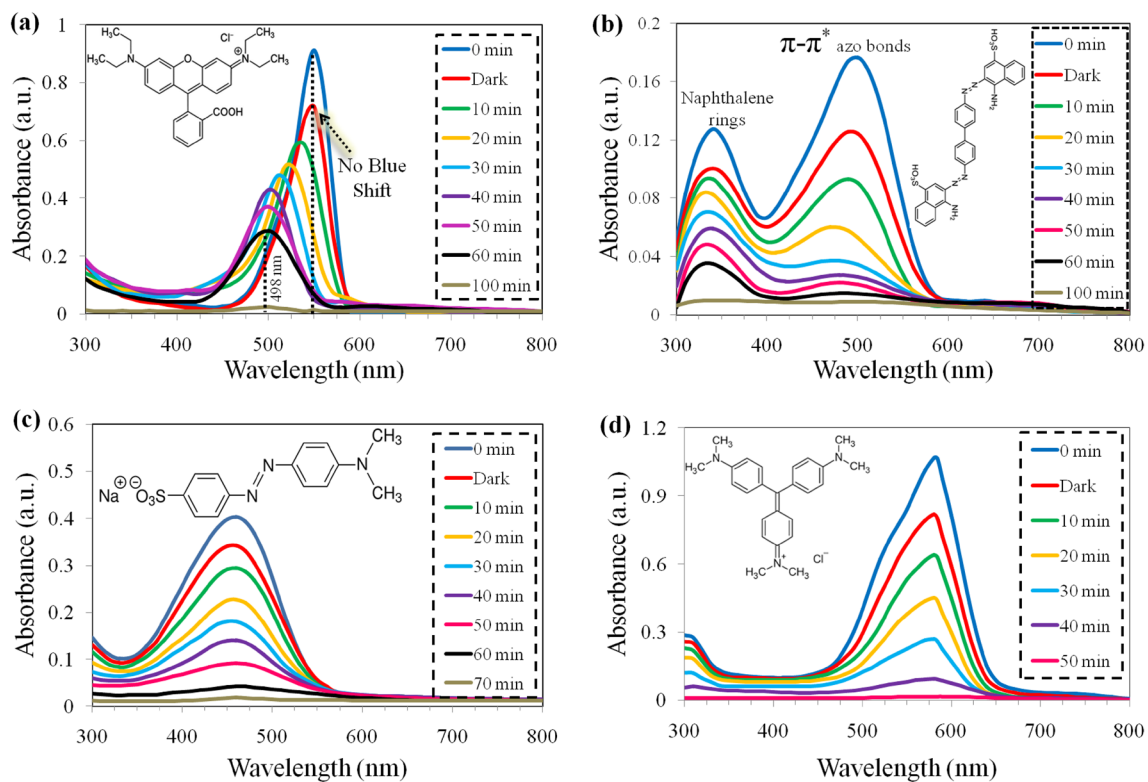


Figure 6. (a) RhB, (b) CR, (c) MO and (d) CV degradation results.

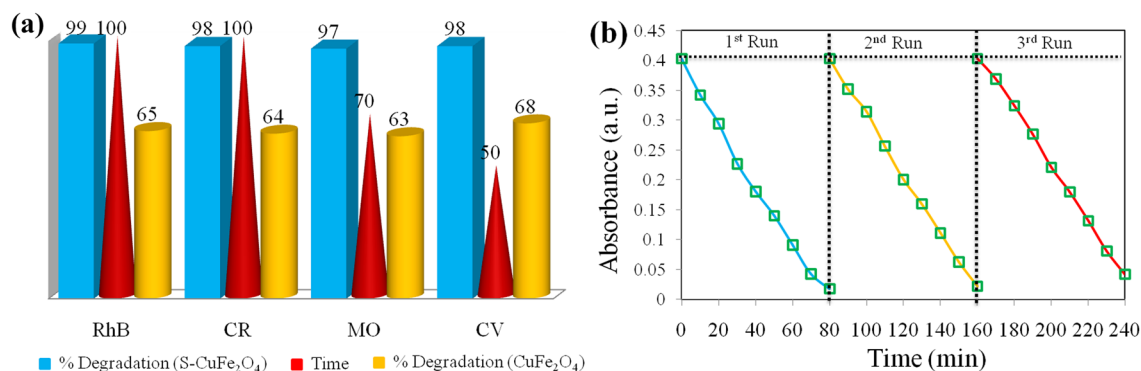


Figure 7. (a) Comparison of % degradation of RhB, CR, MO and CV using pristine (yellow) and S-doped CuFe₂O₄ (blue) photocatalysts and (b) recyclability tests of S-CuFe₂O₄ photocatalysts for MO degradation.

(de-ethylation), due to which the absorbance shifts towards lower wavelength called blue shift. It is observed that λ_{\max} in the graph shifted from 550 to 498 nm. It has been obvious that, blue shift may arise due to energy difference between HOMO and LUMO when rhodamine B is grafted with S-CuFe₂O₄ catalysts. HOMO being filled; its electrons get attracted to the polar S-CuFe₂O₄ by weak dipole-dipole interactions. This attraction lowers the energy of HOMO while empty LUMO energy states of catalysts remain unaffected. This transition shifts the λ_{\max} to the lower wavelength⁶³. Besides this, the appearance of blue shift is due to the step by step N-de-ethylation⁶⁴. This de-ethylation gives rise to N,N,N-triethylrhodamine, N,N-diethyl rhodamine and N-ethyl rhodamine. The final photo-degraded product is assumed to be a completely de-ethylated compound (rhodamine) that has characteristic absorbance maximum at 498 nm⁶⁵.

Figure 6b represents absorption spectra of Congo red (CR) at different time intervals. Photoreaction of CR dye solution by S-CuFe₂O₄ photocatalysts starts after it attains equilibrium between adsorption and desorption in the dark (no light). This adsorption of dye in dark is due to the attraction of two oxygen atoms of sulfonate groups (CR dye) with surfaces of catalysts⁶⁵. This removal is accomplished by parallel decrease in intensity of both peaks without change in their λ_{\max} , that is 340 nm for naphthalene rings and 500 nm for π - π^* azo bonds⁶⁶. After that, it was irradiated with visible light in order to initiate photocatalytic degradation. The absorption spectrum of CR shows two distinct peaks; peak at 500 nm is due to π - π^* azo bonds and second peak at 340 nm is due to naphthalene rings. Actually, π - π^* azo bonds are degraded easily as compared to naphthalene ring. After 100 min, the dye is almost completely removed due to destruction of its chromophoric structure in the vicinity of azo-linkages⁶⁷.

Figure 6c represents absorption spectra of methyl orange (MO). The UV-vis spectra of methyl orange have a distinct broad band in the visible region, with maximum absorption at 460 nm due to the chromophore structure of the dye⁶⁸. It is clear from results that after 70 min, the dye has degraded as a result of photoreaction with S-CuFe₂O₄ photocatalysts. This is due to the destruction of homo- and hetero polyaromatic rings present in methyl orange⁶⁹. It has been investigated that during photoreaction, the -N=N- double bond breaks and simple phenyl rings are formed with amine groups as degraded products⁷⁰.

Crystal violet (CV) degradation is exhibited in Fig. 6d which represents a sharp peak at about 590 nm. Previously reported studies explain that the degradation of crystal violet dye can take place via different mechanisms such as N-demethylation, chromophore cleavage and breaking in ring structure⁷¹. The degradation mechanism and pathway depends on the type of catalysts, degradation method and oxidizing agents used⁷². After 50 min, the violet color of dye solution had completely faded away. The comparative efficiencies of reported ferrites as-well as-prepared S-CuFe₂O₄ are illustrated in the Table 2.

Comparison and recyclability. Figure 7a illustrates the degradation efficiencies of S-doped CuFe₂O₄ in comparison with pristine CuFe₂O₄ for RhB, CR, MO and CV. After 100 min, 99% RhB was degraded by S-doped CuFe₂O₄ but pristine CuFe₂O₄ was able to degrade only 65% of it. Similarly CR was degraded to 98% by S-doped CuFe₂O₄ and 64% by pristine CuFe₂O₄ when measured after 100 min. 97% of MO was degraded by S-doped CuFe₂O₄ and 63% degradation occurred with pristine CuFe₂O₄ after 70 min. For CV, 98% of dye degradation occurred in only 50 min by S-doped CuFe₂O₄ and 68% in presence of pristine CuFe₂O₄. It could be concluded that S-CuFe₂O₄ nanostructures are more efficient photocatalysts as compared to the pristine CuFe₂O₄ because sulphur atoms introduce new active sites that enhance the interactions with the adsorbed dye molecules. Moreover, sulphur dopants modify the electronic structure of the photocatalysts, leading to changes in the bandgap and energy levels. This improves the separation of electron-hole pairs and reduces recombination, leading to more efficient use of the generated charge carriers for dye degradation. Another advantage associated with the use of S-CuFe₂O₄ photocatalysts is its good magnetic properties that allows it to be easily separated from reaction mixture by using external magnet. This separation technique is much easier, faster and efficient as compared to other conventional techniques such as filtration and centrifugation⁸⁶. This also eliminates the risk of secondary pollution from catalysts as well as its full utilization for long times. The recyclability tests were performed for each cycle after careful washing and drying. Figure 7b shows recyclability results of S-CuFe₂O₄ for MO degradation. After being used three times for the degradation of MO, a slight difference in catalyst's efficiency was observed due to loss of catalyst during recovery process.

| Catalyst | Dye | Degradation efficiency (%) | Degradation time (min) | Light source | References |
|--|-----|----------------------------|------------------------|---------------|--------------|
| CuFe ₂ O ₄ | MO | 53 | 90 | UV light | 73 |
| Ce-doped CuFe ₂ O ₄ | MO | 66 | 60 | UV light | 74 |
| Sm-doped CuFe ₂ O ₄ | MO | 66 | 60 | UV light | 75 |
| CoFe ₂ O ₄ | MO | 82 | 90 | UV light | 76 |
| BiFeO ₃ | MO | 86 | 150 | Sunlight | 77 |
| S-CuFe ₂ O ₄ | MO | 97 | 70 | Visible light | Current work |
| C-CuFe ₂ O ₄ | RhB | 30.5 | 360 | Visible light | 78 |
| C-CuFe ₂ O ₄ /ZnO | RhB | 86.9 | 360 | Visible light | 78 |
| NiFe ₂ O ₄ @HAp-Sn ²⁺ | RhB | 84.45 | 60 | Sunlight | 79 |
| S-CuFe ₂ O ₄ | RhB | 99 | 100 | Visible light | Current work |
| NiFe ₂ O ₄ | CR | 96.80 | 60 | Visible light | 80 |
| Mg-Co ferrite | CR | 95.40 | 150 | visible light | 81 |
| Fe ₃ O ₄ | CR | 77 | 60 | Visible light | 82 |
| Cts/Fe ₃ O ₄ | CR | 98 | 60 | Visible light | 82 |
| S-CuFe ₂ O ₄ | CR | 98 | 100 | Visible light | Current work |
| MGF ₃ | CV | 97.67 | 60 | Sunlight | 83 |
| BaFe ₂ O ₄ | CV | 90 | 10 | Microwave | 84 |
| KFe ₄ O ₇ | CV | 92 | 35 | Visible light | 85 |
| S-CuFe ₂ O ₄ | CV | 98 | 50 | Visible light | Current work |

Table 2. Comparison of photocatalysts used for the degradation of dyes.

Mechanism of dye degradation. The degradation mechanism of MO, RhB, CV and CR dyes are shown in Fig. 8. In absence of light, dyes are adsorbed on the surface of photocatalysts. When visible light is irradiated, photoreaction is governed by the excitation of electrons and holes. The electrons start to migrate from valance band to conduction band of photocatalysts. The available electrons at the conduction bands levels readily react with oxygen to generate superoxide radicals ($\cdot\text{O}_2^-$). These superoxide radicals ($\cdot\text{O}_2^-$) react with dyes and convert them to degraded byproducts⁸⁷. At the same time, holes available in valance band levels of catalysts oxidize the dyes over the surfaces of catalysts. Presence of sulphur in the catalysts not only captures electrons but also prevents the recombination of charges (back reaction) and also can produce superoxide radicals ($\cdot\text{O}_2^-$) over active sites of catalyst by transporting electrons to oxygen⁴⁷. Moreover, holes oxidize the H₂O molecules into $\cdot\text{OH}$ radicals, these hydroxyl radicals further enhance the dye adsorption at the surfaces of catalysts^{88,89}. Due to higher dye adsorption at catalysts surfaces, rate of dye degradation is readily increased (Scheme 1).

Conclusion

In this work, CuFe₂O₄ and S-CuFe₂O₄ photocatalysts were successfully synthesized by employing hydrothermal methods. For structural morphologies XRD, Raman and FT-IR techniques were subjected to confirm crystallinity and sulphur doping. The results depicts that the doping of non-metallic anionic sulphur causes strain in the lattice and enter the lattice as anions by replacing oxygen. SEM results confirm that sulphur doping reduces the agglomeration and increases the actives cites for photoreactions. EDX confirms the presence of sulphur whereas

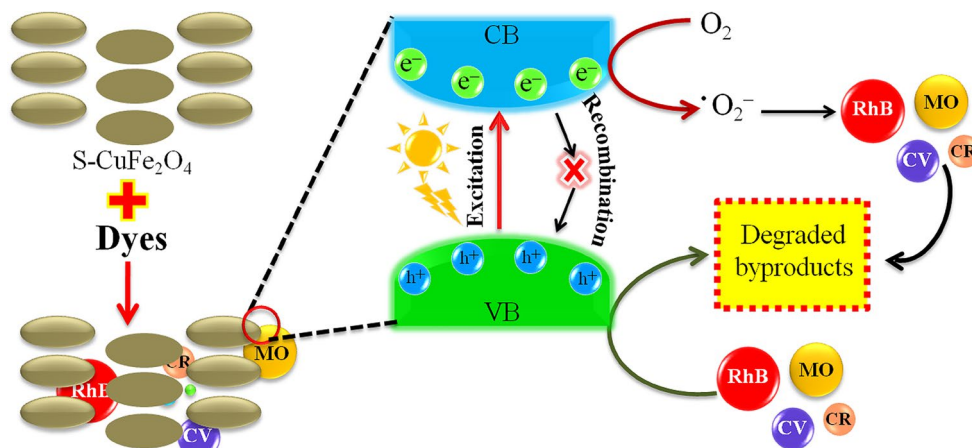
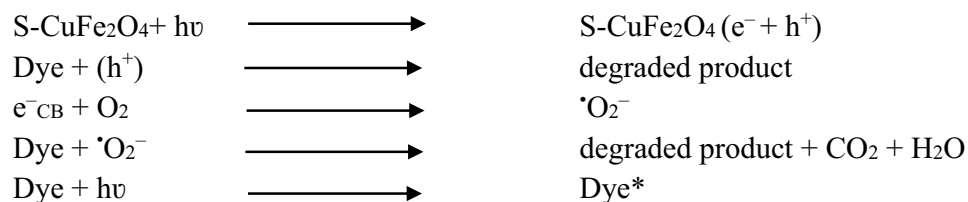


Figure 8. Photocatalytic dye degradation reaction over S-CuFe₂O₄ photocatalysts.



Scheme 1. Photocatalytic reactions involved in dye degradation.

TGA confirms the stability of as-synthesised S-CuFe₂O₄ at higher temperatures. PL results gave evidences that sulphur was capable to act as electron trapping centre which suppressed the recombination of charges during the photoexcitation. The CuFe₂O₄ and S-CuFe₂O₄ photocatalysts were used to degrade RhB, CR, MO and CV dyes, results revealed that doping of sulphur boosts the photocatalytic degradation reactions. It has been found that by using S-CuFe₂O₄, RhB degradation efficiency has been increased from 65 to 99% within 100 min. The dye degradation results of this work assure the superior performances of S-CuFe₂O₄ than pristine CuFe₂O₄. On the basis of photocatalytic efficiencies, this work can be assigned as excellent candidate for photocatalysis applications.

Data availability

All data used and analyzed in current work are included in this article and SI file.

Received: 20 December 2022; Accepted: 8 April 2023

Published online: 18 April 2023

References

- Ahmed, J., Thakur, A. & Goyal, A. *Industrial Wastewater and Its Toxic Effects* (2021).
- Khairnar, S. D. & Shrivastava, V. S. Facile synthesis of nickel oxide nanoparticles for the degradation of methylene blue and Rhodamine B dye: A comparative study. *J. Taibah Univ. Sci.* **13**(1), 1108–1118 (2019).
- Khairnar, S. D. *et al.* Adsorptive and photocatalytic removal of carcinogenic methylene blue dye by SnO₂ nanorods: An equilibrium, kinetic and thermodynamics exploration. *SN Appl. Sci.* **2**, 1–12 (2020).
- Raval, N. P., Shah, P. U. & Shah, N. K. Adsorptive amputation of hazardous azo dye Congo red from wastewater: A critical review. *Environ. Sci. Pollut. Res.* **23**(15), 14810–14853 (2016).
- Mittal, A. *et al.* Adsorptive removal of hazardous anionic dye “Congo red” from wastewater using waste materials and recovery by desorption. *J. Colloid Interface Sci.* **340**(1), 16–26 (2009).
- Culp, S. *et al.* Mutagenicity and carcinogenicity in relation to DNA adduct formation in rats fed leucomalachite green. *Mutat. Res./Fundam. Mol. Mech. Mutagen.* **506**, 55–63 (2002).
- Haque, E. *et al.* Adsorptive removal of methyl orange from aqueous solution with metal-organic frameworks, porous chromium-benzenedicarboxylates. *J. Hazard. Mater.* **181**(1–3), 535–542 (2010).
- Rai, A. *et al.* Sustainable treatment of dye wastewater by recycling microalgal and diatom biogenic materials: Biorefinery perspectives. *Chemosphere*, **305**, 135371 (2022).
- Lv, X., Lam, F. L. Y. & Hu, X. A review on bismuth oxyhalide (BiOX, X= Cl, Br, I) based photocatalysts for wastewater remediation. *Front. Catal.* **2**, 4 (2022).
- Srivastava, V. *et al.* Green synthesis of biogenic silver particles, process parameter optimization and application as photocatalyst in dye degradation. *SN Appl. Sci.* **1**, 1–15 (2019).
- Singh, P. K. & Singh, R. L. Bio-removal of azo dyes: A review. *Int. J. Appl. Sci. Biotechnol.* **5**(2), 108–126 (2017).
- Bhatia, S. K. *et al.* Wastewater based microalgal biorefinery for bioenergy production: Progress and challenges. *Sci. Total Environ.* **751**, 141599 (2021).
- Khairnar, S. D. & Shrivastava, V. S. Photocatalytic degradation of chlorpyrifos and methylene blue using $\alpha\text{-Bi}_2\text{O}_3$ nanoparticles fabricated by sol–gel method. *SN Appl. Sci.* **1**, 1–10 (2019).
- Yadav, S. *et al.* A review on degradation of organic dyes by using metal oxide semiconductors. *Environ. Sci. Pollut. Res.* **29**, 1–21 (2022).
- Yang, Q. & Hao, J. Synthesis of metal sulfides via ionic liquid-mediated assembly strategy and their photocatalytic degradation of dyes in water. *Colloids Surf. A* **633**, 127848 (2022).
- Alshorifi, F. T., Alswat, A. A. & Salama, R. S. Gold-selenide quantum dots supported onto cesium ferrite nanocomposites for the efficient degradation of rhodamine B. *Heliyon* **8**(6), e09652 (2022).
- Lu, Q. *et al.* Photocatalytic degradation of methyl orange by noble metal Ag modified semiconductor Zn₂SnO₄. *Mater. Sci. Semicond. Process.* **138**, 106290 (2022).
- Du, X.-H. *et al.* BODIPY-linked conjugated porous polymers for dye wastewater treatment. *Microporous Mesoporous Mater.* **332**, 111711 (2022).
- Dake, D. *et al.* Photocatalytic performance of graphene-based Cr-substituted β ZnS nanocomposites. *Appl. Phys. A* **128**(4), 1–20 (2022).
- Chandra, S. *et al.* Highly luminescent gold nanocluster frameworks. *Adv. Opt. Mater.* **7**(20), 1900620 (2019).
- Ali, N. *et al.* Enhanced photodegradation of methylene blue with alkaline and transition-metal ferrite nanophotocatalysts under direct sun light irradiation. *J. Chin. Chem. Soc.* **66**(4), 402–408 (2019).
- Gnanamoorthy, G. *et al.* Photocatalytic properties of amine functionalized Bi₂Sn₂O₇/rGO nanocomposites. *J. Phys. Chem. Solids* **118**, 21–31 (2018).
- Gnanamoorthy, G. *et al.* Global popularization of CuNiO₂ and their rGO nanocomposite loaded to the photocatalytic properties of methylene blue. *Environ. Res.* **204**, 112338 (2022).
- Abid, Z. *et al.* Synergism of Co/Na in BiVO₄ microstructures for visible-light driven degradation of toxic dyes in water. *Nanoscale Adv.* **5** (2023).
- Gnanamoorthy, G. *et al.* New orchestrated of X-CuTiAP (en, trien, ETA and DMA) nanospheres with enhanced photocatalytic and antimicrobial activities. *J. Ind. Eng. Chem.* **110**, 503–519 (2022).

26. Patil, M. R., Khairnar, S. D. & Shrivastava, V. Synthesis, characterisation of polyaniline-Fe₃O₄ magnetic nanocomposite and its application for removal of an acid violet 19 dye. *Appl. Nanosci.* **6**(4), 495–502 (2016).
27. Sugimoto, M. The past, present, and future of ferrites. *J. Am. Ceram. Soc.* **82**(2), 269–280 (1999).
28. Ding, R.-R. *et al.* Oxygen vacancy on hollow sphere CuFe₂O₄ as an efficient Fenton-like catalysis for organic pollutant degradation over a wide pH range. *Appl. Catal. B* **291**, 120069 (2021).
29. Prashanth, P. *et al.* Synthesis, characterizations, antibacterial and photoluminescence studies of solution combustion-derived α-Al₂O₃ nanoparticles. *J. Asian Ceram. Soc.* **3**(3), 345–351 (2015).
30. Arifin, M. N. *et al.* Synthesis of titania doped copper ferrite photocatalyst and its photoactivity towards methylene blue degradation under visible light irradiation. *Bull. Chem. React. Eng. Catal.* **14**(1), 219 (2019).
31. Amulya, M. S. *et al.* Evaluation of bifunctional applications of CuFe₂O₄ nanoparticles synthesized by a sonochemical method. *J. Phys. Chem. Solids* **148**, 109756 (2021).
32. Kharisov, B. I., Dias, H. R. & Kharissova, O. V. Mini-review: Ferrite nanoparticles in the catalysis. *Arab. J. Chem.* **12**(7), 1234–1246 (2019).
33. Khairnar, S. D., Patil, M. R. & Shrivastava, V. S. Hydrothermally synthesized nanocrystalline Nb₂O₅ and its visible-light photocatalytic activity for the degradation of congo red and methylene blue. *Iran. J. Catal.* **8**(2), 143–150 (2018).
34. Koli, P. B. *et al.* Transition metal incorporated, modified bismuth oxide (Bi₂O₃) nano photo catalyst for deterioration of rosaniline hydrochloride dye as resource for environmental rehabilitation. *J. Indian Chem. Soc.* **98**(11), 100225 (2021).
35. Li, R. *et al.* Construction of heterostructured CuFe₂O₄/g-C₃N₄ nanocomposite as an efficient visible light photocatalyst with peroxydisulfate for the organic oxidation. *Appl. Catal. B* **244**, 974–982 (2019).
36. Zhao, W. *et al.* A simple method for fabricating p–n junction photocatalyst CuFe₂O₄/Bi₄Ti₃O₁₂ and its photocatalytic activity. *Mater. Chem. Phys.* **143**(3), 952–962 (2014).
37. Keerthana, S. *et al.* Pure and Ce-doped spinel CuFe₂O₄ photocatalysts for efficient rhodamine B degradation. *Environ. Res.* **200**, 111528 (2021).
38. Dayana, P. N. *et al.* Zirconium doped copper ferrite (CuFe₂O₄) nanoparticles for the enhancement of visible light-responsive photocatalytic degradation of rose Bengal and indigo carmine dyes. *J. Cluster Sci.* **33**(4), 1739–1749 (2022).
39. Pallavolu, M. R. *et al.* Bio-derived graphitic carbon quantum dot encapsulated S- and N-doped graphene sheets with unusual battery-type behavior for high-performance supercapacitor. *Carbon* **202**, 93–102 (2023).
40. Qin, X. *et al.* Nitrogen- and sulfur-doped graphene quantum dots for chemiluminescence. *Nanoscale* **5**(8), 3864–3871 (2023).
41. Rati, Y. *et al.* Visible light assisted degradation of Rhodamin B by reusable S-doped ZnO thin film photocatalyst. *Opt. Mater.* **135**, 113370 (2023).
42. Patil, A. B., Patil, K. R. & Pardeshi, S. K. Ecofriendly synthesis and solar photocatalytic activity of S-doped ZnO. *J. Hazard. Mater.* **183**(1), 315–323 (2010).
43. Sreekala, G. *et al.* Removal of lead (II) ions from water using copper ferrite nanoparticles synthesized by green method. *Mater. Today Proc.* **45**, 3986–3990 (2021).
44. Rezaul Karim, K. M. *et al.* Photoelectrocatalytic reduction of carbon dioxide to methanol using CuFe₂O₄ modified with graphene oxide under visible light irradiation. *Ind. Eng. Chem. Res.* **58**(2), 563–572 (2019).
45. Khairnar, S. D. *et al.* Synthesis and characterization of 2-D La-doped Bi₂O₃ for photocatalytic degradation of organic dye and pesticide. *J. Photochem. Photobiol.* **6**, 100030 (2021).
46. Kumar, A. *et al.* Greener route for synthesis of aryl and alkyl-14H-dibenzo [a]j xanthenes using graphene oxide-copper ferrite nanocomposite as a recyclable heterogeneous catalyst. *Sci. Rep.* **7**(1), 1–18 (2017).
47. Mirzaeifard, Z. *et al.* ZnO photocatalyst revisited: Effective photocatalytic degradation of emerging contaminants using S-doped ZnO nanoparticles under visible light radiation. *Ind. Eng. Chem. Res.* **59**(36), 15894–15911 (2020).
48. Luo, L. *et al.* High lithium electroactivity of electrospun CuFe₂O₄ nanofibers as anode material for lithium-ion batteries. *Electrochim. Acta* **144**, 85–91 (2014).
49. Maleki, A., Hajizadeh, Z. & Salehi, P. Mesoporous halloysite nanotubes modified by CuFe₂O₄ spinel ferrite nanoparticles and study of its application as a novel and efficient heterogeneous catalyst in the synthesis of pyrazolopyridine derivatives. *Sci. Rep.* **9**(1), 1–8 (2019).
50. Hoa, P. *et al.* Gas sensing properties of CuFe₂O₄ nanoparticles prepared by spray co-precipitation method. *Vietnam J. Chem.* **57**, 32–38 (2019).
51. Oliveira, T. P. *et al.* Synthesis, characterization, and photocatalytic investigation of CuFe₂O₄ for the degradation of dyes under visible light. *Catalysts* **12**(6), 623 (2022).
52. Hussain, E. *et al.* Titania-supported palladium/strontium nanoparticles (Pd/Sr-NPs@P25) for photocatalytic H₂ production from water splitting. *J. Phys. Chem. C* **120**(31), 17205–17213 (2016).
53. Attia, S. *et al.* Effect of Ni toward the optical and transport properties of the spinel solid solution Ni_xCu_{1-x}Fe₂O₄ nanoparticles. *J. Environ. Chem. Eng.* **10**(6), 108601 (2022).
54. Selima, S. S., Khairy, M. & Mousa, M. A. Comparative studies on the impact of synthesis methods on structural, optical, magnetic and catalytic properties of CuFe₂O₄. *Ceram. Int.* **45**(5), 6535–6540 (2019).
55. Amuthan, T. *et al.* A novel p-CuFe₂O₄/n-ZnS heterojunction photocatalyst: Co-precipitation synthesis, characterization and improved visible-light driven photocatalytic activity for removal of MB and CV dyes. *Phys. B* **638**, 413842 (2022).
56. Link, S. & El-Sayed, M. A. Shape and size dependence of radiative, non-radiative and photothermal properties of gold nanocrystals. *Int. Rev. Phys. Chem.* **19**(3), 409–453 (2000).
57. Hammad, T. M. *et al.* Optical and magnetic characterizations of zinc substituted copper ferrite synthesized by a co-precipitation chemical method. *J. Alloy. Compd.* **741**, 123–130 (2018).
58. Graetzel, M. *et al.* Materials interface engineering for solution-processed photovoltaics. *Nature* **488**(7411), 304–312 (2012).
59. Hussain, E. *et al.* Remarkable effect of BaO on photocatalytic H₂ evolution from water splitting via TiO₂ (P25) supported palladium nanoparticles. *J. Environ. Chem. Eng.* **7**(1), 102729 (2019).
60. Qian, R. *et al.* Charge carrier trapping, recombination and transfer during TiO₂ photocatalysis: An overview. *Catal. Today* **335**, 78–90 (2019).
61. Chang, S. *et al.* High-efficiency and selective adsorption of organic pollutants by magnetic CoFe₂O₄/graphene oxide adsorbents: Experimental and molecular dynamics simulation study. *Sep. Purif. Technol.* **238**, 116400 (2020).
62. Liu, T. *et al.* Molecular structure perspective on Temperature-Sensitive properties of rhodamine aqueous solutions. *Spectrochim. Acta Part A Mol. Biomol. Spectrosc.* **275**, 121166 (2022).
63. Shao, Y. *et al.* The photoluminescence of rhodamine B encapsulated in mesoporous Si-MCM-48, Ce-MCM-48, Fe-MCM-48 and Cr-MCM-48 molecular sieves. *J. Photochem. Photobiol. A* **180**(1), 59–64 (2006).
64. Zhong, H. *et al.* Microwave photocatalytic degradation of Rhodamine B using TiO₂ supported on activated carbon: Mechanism implication. *J. Environ. Sci.* **21**(2), 268–272 (2009).
65. Zhuang, J. *et al.* Photocatalytic degradation of RhB over TiO₂ bilayer films: Effect of defects and their location. *Langmuir* **26**(12), 9686–9694 (2010).
66. Malwal, D. & Gopinath, P. Enhanced photocatalytic activity of hierarchical three dimensional metal oxide@CuO nanostructures towards the degradation of Congo red dye under solar radiation. *Catal. Sci. Technol.* **6**(12), 4458–4472 (2016).

67. Movahedi, M., Mahjoub, A. R. & Janitabar-Darzi, S. Photodegradation of Congo red in aqueous solution on ZnO as an alternative catalyst to TiO₂. *J. Iran. Chem. Soc.* **6**(3), 570–577 (2009).
68. Lü, X.-F. *et al.* Degradation of methyl orange by UV, O₃ and UV/O₃ systems: Analysis of the degradation effects and mineralization mechanism. *Res. Chem. Intermed.* **39**(9), 4189–4203 (2013).
69. Basahel, S. N. *et al.* Influence of crystal structure of nanosized ZrO₂ on photocatalytic degradation of methyl orange. *Nanoscale Res. Lett.* **10**(1), 73 (2015).
70. Sha, Y. *et al.* Rapid degradation of azo dye methyl orange using hollow cobalt nanoparticles. *Chemosphere* **144**, 1530–1535 (2016).
71. Zhang, Y. *et al.* Oxidation characteristics and degradation potential of a dye-decolorizing peroxidase from *Bacillus amyloliquefaciens* for crystal violet dye. *Biochem. Eng. J.* **168**, 107930 (2021).
72. Soliman, A. M. *et al.* Photocatalytic activity of transition metal ions-loaded activated carbon: Degradation of crystal violet dye under solar radiation. *J. Water Process Eng.* **17**, 245–255 (2017).
73. Vosoughifar, M. Preparation and application of copper ferrite nanoparticles for degradation of methyl orange. *J. Mater. Sci. Mater. Electron.* **27**(10), 10449–10453 (2016).
74. Rahimi-Nasrabadi, M. *et al.* Nanocrystalline Ce-doped copper ferrite: Synthesis, characterization, and its photocatalyst application. *J. Mater. Sci. Mater. Electron.* **27**(11), 11691–11697 (2016).
75. Ahmadi, H. *et al.* Nanocrystalline CuFe_{2–x}Sm_xO₄: Synthesis, characterization and its photocatalytic degradation of methyl orange. *J. Mater. Sci. Mater. Electron.* **27**(5), 4689–4693 (2016).
76. Nasiri, A. *et al.* Nanocrystalline copper ferrite: Synthesis of different shapes through a new method and its photocatalyst application. *J. Mater. Sci. Mater. Electron.* **28**(3), 2401–2406 (2017).
77. Ruby, S. *et al.* Sunlight-driven photocatalytic degradation of methyl orange based on bismuth ferrite (BiFeO₃) heterostructures composed of interconnected nanosheets. *J. Nanosci. Nanotechnol.* **20**(3), 1851–1858 (2020).
78. Lu, C. *et al.* Facile fabrication of heterostructured cubic-CuFe₂O₄/ZnO nanofibers (c-CFZs) with enhanced visible-light photocatalytic activity and magnetic separation. *RSC Adv.* **6**(111), 110155–110163 (2016).
79. Das, K. C. *et al.* Sn (II) inserted on hydroxyapatite encapsulated nickel ferrite (NiFe₂O₄@HAP-Sn²⁺): A novel nanocomposite for the effective photo-degradation of rhodamine B dye. *J. Clean. Prod.* **290**, 125172 (2021).
80. Hariani, P. L. *et al.* Preparation of NiFe₂O₄ nanoparticles by solution combustion method as photocatalyst of Congo red. *Bull. Chem. React. Eng. Catal.* **16**(3), 481–490 (2021).
81. Jadhav, S. D. & Patil, R. Photocatalytic degradation study of Methyl Orange and Congo red using Mg-Co ferrite powder. *J. Water Environ. Nanotechnol.* **7**(2), 170–179 (2022).
82. Maruthupandy, M. *et al.* Development of chitosan decorated Fe₃O₄ nanospheres for potential enhancement of photocatalytic degradation of Congo red dye molecules. *Spectrochim. Acta Part A Mol. Biomol. Spectrosc.* **267**, 120511 (2022).
83. Jasrotia, R. *et al.* Robust and sustainable Mg_{1-x}Ce_xNi_yFe_{2-y}O₄ magnetic nanophotocatalysts with improved photocatalytic performance towards photodegradation of crystal violet and rhodamine B pollutants. *Chemosphere* **294**, 133706 (2022).
84. Liu, X. *et al.* Microwave-assisted catalytic degradation of crystal violet with barium ferrite nanomaterial. *Ind. Eng. Chem. Res.* **55**(46), 11869–11877 (2016).
85. Zhang, X. *et al.* Potassium ferrite as heterogeneous photo-fenton catalyst for highly efficient dye degradation. *Catalysts* **10**(3), 293 (2020).
86. Masunga, N. *et al.* Recent advances in copper ferrite nanoparticles and nanocomposites synthesis, magnetic properties and application in water treatment: Review. *J. Environ. Chem. Eng.* **7**(3), 103179 (2019).
87. Konstantinou, I. K. & Albanis, T. A. TiO₂-assisted photocatalytic degradation of azo dyes in aqueous solution: Kinetic and mechanistic investigations: A review. *Appl. Catal. B* **49**(1), 1–14 (2004).
88. Rao, Z. *et al.* Photocatalytic oxidation mechanism of Gas-Phase VOCs: Unveiling the role of holes, ·OH and ·O²⁻. *Chem. Eng. J.* **430**, 132766 (2022).
89. Ilyas, A. *et al.* Growth of villi-microstructured bismuth vanadate (Vm-BiVO₄) for photocatalytic degradation of crystal violet dye. *RSC Adv.* **13**(4), 2379–2391 (2023).

Acknowledgements

This work was financially supported by Higher Education Commission (HEC) of Pakistan (No. 377/IPFP-II) (Batch-I)/SRGP/NAHE/HEC/2020/27 Islamabad. Synthesis work and dye degradation activities were conducted in Institute of Chemistry, The Islamia University of Bahawalpur (Inorganic Material Laboratory (52s)). Dr. Ejaz Hussain acknowledges Syed Babar Ali School of Science and engineering, Lahore University of Management Sciences (LUMS) to facilitate for characterization of samples.

Author contributions

A.A and M.Z.A completed the synthesis work. K.R prepared and edited manuscript, A.R facilitated characterization of samples. E.H supervised the work, finalized and submitted the manuscript.

Competing interests

The authors declare no competing interests.

Additional information

Supplementary Information The online version contains supplementary material available at <https://doi.org/10.1038/s41598-023-33185-0>.

Correspondence and requests for materials should be addressed to E.H.

Reprints and permissions information is available at www.nature.com/reprints.

Publisher's note Springer Nature remains neutral with regard to jurisdictional claims in published maps and institutional affiliations.



Open Access This article is licensed under a Creative Commons Attribution 4.0 International License, which permits use, sharing, adaptation, distribution and reproduction in any medium or format, as long as you give appropriate credit to the original author(s) and the source, provide a link to the Creative Commons licence, and indicate if changes were made. The images or other third party material in this article are included in the article's Creative Commons licence, unless indicated otherwise in a credit line to the material. If material is not included in the article's Creative Commons licence and your intended use is not permitted by statutory regulation or exceeds the permitted use, you will need to obtain permission directly from the copyright holder. To view a copy of this licence, visit <http://creativecommons.org/licenses/by/4.0/>.

© The Author(s) 2023